

# Physical Perception Network and an All-weather Multi-modality Benchmark for Adverse Weather Image Fusion

Xilai Li\* Wuyang Liu\* Xiaosong Li† Haishu Tan

School of Physics and Optoelectronic Engineering, Foshan University, Foshan 528225, China

20210300236@stu.fosu.edu.cn, lixiaosong@buaa.edu.cn



Figure 1. The proposed method can achieve high-quality multi-modality image fusion under various adverse weather conditions. The left and right are the heavy snow-covered visible and infrared images, respectively, the middle is the fused image.

## Abstract

*Multi-modality image fusion (MMIF) integrates the complementary information from different modal images to provide comprehensive and objective interpretation of a scenes. However, existing MMIF methods lack the ability to resist different weather interferences in real-life scenarios, preventing them from being useful in practical applications such as autonomous driving. To bridge this research gap, we proposed an all-weather MMIF model. Regarding deep learning architectures, their network designs are often viewed as a black box, which limits their multitasking capabilities. For deweathering module, we propose a physically-aware clear feature prediction module based on an atmospheric scattering model that can deduce variations in light transmittance from both scene illumination and depth. For fusion module, We utilize a learnable low-rank representation model to decompose images into low-rank and sparse components. This highly interpretable feature separation allows us to better observe and understand images. Furthermore, we have established a benchmark for MMIF research under extreme weather conditions. It encompasses*

*multiple scenes under three types of weather: rain, haze, and snow, with each weather condition further subdivided into various impact levels. Extensive fusion experiments under adverse weather demonstrate that the proposed algorithm has excellent detail recovery and multi-modality feature extraction capabilities.*

## 1. Introduction

Infrared and visible image fusion (IVIF) is performed to integrate the complementary and salient feature information from different modal images to achieve a more comprehensive interpretation of a target scene. By integrating data from different spectral ranges, IVIF contributes to advancements in computer vision tasks [16, 20, 21, 43], including semantic segmentation [2, 3, 18], object detection [1, 33, 34], video surveillance [25], and unmanned driving [37]. Recently, deep learning (DL) has exhibited remarkable progress within the realm of artificial intelligence owing to its exceptional aptitude for intricate nonlinear approximations and adeptness in extracting salient features. Consequently, several highly efficient algorithms tailored to the IVIF domain have been developed. These algorithms can be broadly categorized into three groups: generative adversar-

\*Equal contribution.

†Corresponding author.

ial networks (GAN)-based models [9, 14, 23, 45], autoencoder (AE)-based models [10, 19, 24, 32, 43], and algorithmic expansion models [7, 16, 42].

Each of these methodologies has achieved commendable outcomes in the IVIF field. However, there are three key questions that remain unanswered in this field.

- Currently, there is a critical research gap in that IVIF cannot deliver robust scene information under adverse weather conditions. Addressing this challenge requires more than isolated algorithmic solutions for specific weather-related issues, necessitating a unified framework to comprehensively restore intricate scene details affected by adverse weather.
- The network design of most current DL-based methods, which are primarily developed using empirical and experiential approaches, are not highly interpretable owing to their black box nature. Therefore, identifying an appropriate framework is time-consuming. An alternative strategy involves structuring networks guided by mathematical optimization principles or physical models, offering the potential for increased efficiency and interpretability in network design.
- Generally, DL-based algorithms are driven by data. Existing datasets dedicated to collecting comprehensive imaging data from multiple modalities are complete in terms of scene diversity. However, no large datasets have been developed specifically for research on applying IVIF to scenarios with adverse weather conditions. Even if certain datasets can cover scenes affected by rain and haze, their limited data make it difficult to employ them for training in joint image restoration and fusion.

To address above challenges, we propose an all-weather MMIF algorithm (AWFusion) that integrates both deweathering and fusion functions within a single framework, thereby providing an effective means to achieve robust fusion under adverse weather conditions. According to the physical imaging model, different weather effects have some common features, i.e., there will be common degradation in images taken under different severe weather conditions [46], which gives us a research basis to realize deweathering in the same framework. In the deweathering module, guided by the atmospheric scattering model [8, 44], the basic framework of a detailed prediction module was constructed. Here, the illumination and depth features of images were derived to predict the distribution of light transmission features based on learned convolutional sparse coding (LCSC) [29]. Thus, propelled by both mathematical optimization algorithms and physical models, our proposed model has highly interpretable and physically-aware properties. It obviates the necessity for model customization to cater to specific weather-related issues, and it enables the simultaneous training of multiple teacher networks under a unified framework for a singular weather restoration task.

Subsequently, distillation learning was incorporated into the model to transfer knowledge from these diverse teacher networks to a singular student network, enabling the model to identify and resolve degradation issues stemming from various severe weather phenomena.

The fusion module was constructed to equip the network with the ability to extract multi-modality information, isolate the shared and unique features of each modality, and fuse them based on a unique prior for each feature type. Firstly, we introduce a learned low-rank representation (LLRR) block [16] to decompose the source images into sparse and low-rank components. A sparse feature prediction module based on an optimization model was proposed to reconstruct the sparse components, and a new sparse transformer [6] was introduced to capture the long-range contextual information of an image. The contributions of this study are summarized as follows.

- We propose an end-to-end all-weather MMIF framework, effectively fusing and recovering the perturbed multi-modality information. **Unlike existing MMIF works, to the best of our knowledge, this is the first work to address MMIF and adverse weather removal simultaneously, defining a new challenging task.**
- We propose a physically-aware clear feature prediction block (PFB) that comprehensively accounts for the restoration of clear features, thereby avoiding a time-consuming empirical network design. We evaluate recovered images from the perspective of image depth information recovery and construct semantic loss.
- We propose a feature separation-based fusion module that considers the reconstruction of local and global features from sparse and low-rank components. Additionally, we develop an anti-interference interactive perceptual learning strategy (APLS), enhancing the network’s capability to effectively remove interfering pixels.
- Leveraging both existing MMIF datasets and our collected data, we built a dataset (AWMM-100k) dedicated to MMIF research under adverse weather. It contains 100,000 aligned infrared and visible image pairs with labels for object detection, establishing it as a versatile benchmark for a broad spectrum of vision tasks.

## 2. Related Work

### 2.1. DL-based MMIF Methods

DL-based IVIF algorithms [13, 22, 38, 40, 41] demonstrate robust fusion performance in conventional scenes, employing methodologies such as GAN or AE to effectively integrate salient feature information from each modality. With the widespread utilization of IVIF technology, researchers increasingly integrate this technology into downstream vision tasks [17, 20, 30]. Their aim is to enhance the extraction of multi-modality features, augmenting semantic infor-

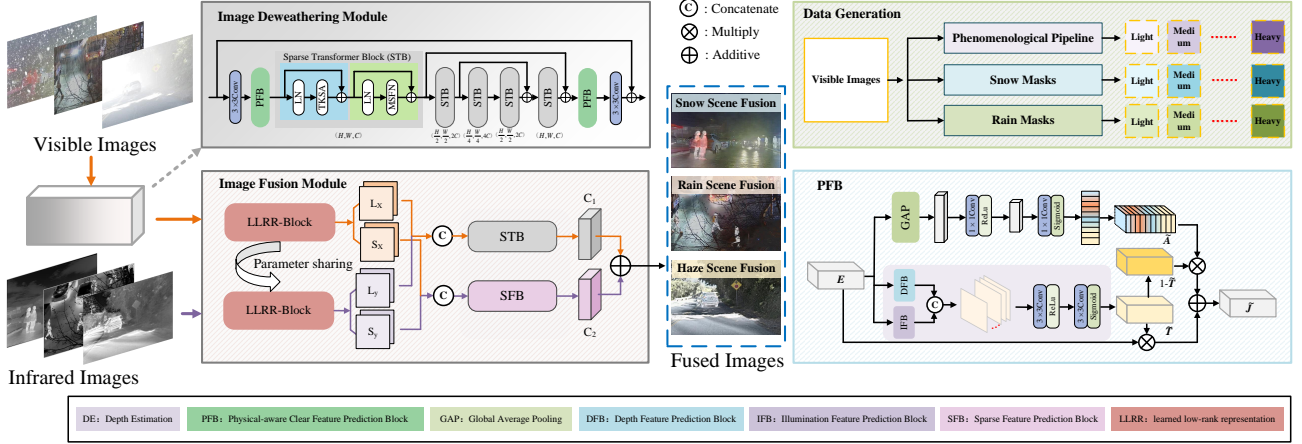


Figure 2. The architecture of the proposed all-weather multi-modality image fusion framework.

mation and leveraging fused images to optimize the performance of tasks such as object detection, semantic segmentation, and salient object detection. Furthermore, in practical applications, images captured by cameras may be slightly misaligned and distorted; some researchers have designed correction networks for fusion specifically for such situations [11]. Xu et al. [39] designed an IVIF model that could fuse unaligned image pairs, effectively reducing the cost of adopting IVIF technology. In some cases, the fixed input and output resolutions of images can limit the development of IVIF-based methods; Li et al. [15] designed an IVIF framework specifically for this problem. Currently, existing research does not consider effectively generalizing IVIF algorithms, regardless of whether they are single- or multi-tasking algorithms, to adverse weather scenes.

### 3. Proposed Method

As shown in the Fig. 2, AWFusion comprises two main stages: image deweathering and image fusion.

#### 3.1. Image Deweathering Module

The first phase aims to achieve image restoration in the presence of three types of adverse weather conditions (rain, snow, and haze) and implement it using a unified framework with only one pretrained weight. Drawing inspiration from Che et al. [5], we introduced a distillation learning approach in which distinct teacher models are initially trained for individual weather-related issues. Subsequently, knowledge is collaboratively transferred from these multiple teacher models to student models to comprehensively address weather-related challenges. Additionally, for the deweathering module, an atmospheric scattering model was combined to simulate the process of image degradation, and a physically-aware PFB was proposed.

#### 3.1.1 PFB

The construction of the PFB was guided by the physical mechanism of image degradation and transformation of the atmospheric scattering model. First, utilizing kernel  $k$  for feature extraction results in the following revised expression of atmospheric scattering model:

$$k \cdot J = k \cdot (I \odot \frac{1}{T}) + k \cdot A - k \cdot (A \odot \frac{1}{T}) \quad (1)$$

where  $*$  denotes the convolution operator, and  $\odot$  represents the Hadamard product. Subsequently, by introducing the matrix-vector forms of  $k$ ,  $J$ ,  $I$ ,  $A$ , and  $1/T$ , which are denoted as  $\mathbf{K}$ ,  $\mathbf{J}$ ,  $\mathbf{I}$ ,  $\mathbf{A}$ , and  $\mathbf{D}$ , respectively, Eq. (1) can be redefined as follows:

$$\mathbf{KJ} = \mathbf{KDI} + \mathbf{KA} - \mathbf{KDA} \quad (2)$$

According to [44], given the input adverse weather image feature  $E \in \mathbb{R}^{H \times W \times K}$ , the clear feature  $\tilde{J} \in \mathbb{R}^{H \times W \times K}$  can be computed as follows:

$$\tilde{\mathbf{J}} = \mathbf{E} \odot \tilde{\mathbf{T}} + \tilde{\mathbf{A}}(1 - \tilde{\mathbf{T}}) \quad (3)$$

where  $\tilde{\mathbf{A}} \in \mathbb{R}^{H \times W \times K}$  represents an approximation of the characteristic  $\mathbf{KA}$  of the atmospheric light  $A$ , and  $\tilde{\mathbf{T}} \in \mathbb{R}^{H \times W \times K}$  is a characteristic associated with the transmission map.  $1$  represents a matrix composed entirely of ones. Since atmospheric light is usually assumed to be homogeneous, as shown in Fig. 2, we use global average pooling to eliminate redundant information within the feature space to predict the atmospheric light feature  $\tilde{\mathbf{A}}$ .

For the prediction of the feature  $\tilde{\mathbf{T}}$ , we believe that by analyzing changes in depth and illumination of objects in an image, we can infer changes in light transmission, thus realizing estimation of the image transmission information.

Consequently, we disassemble  $\tilde{\mathbf{T}}$  into a combination of depth  $d_k \in \mathbb{R}^{H \times W \times K}$  and illumination  $m_k \in \mathbb{R}^{H \times W \times K}$  features, which is modeled as follows:

$$\tilde{\mathbf{T}} = \sum_k g_k^d \cdot d_k + \sum_k g_k^i \cdot i_k \quad (4)$$

where  $\{g_k^d\}_{k=1}^K \in \mathbb{R}^{s \times s \times K}$  and  $\{g_k^m\}_{k=1}^K \in \mathbb{R}^{s \times s \times K}$  are the depth and illumination filters of  $\tilde{\mathbf{T}}$ , respectively, and  $K$  denotes the number of filters. Subsequently, we compute the depth and illumination feature responses  $\{d_k, i_k\}_{k=1}^K$  by solving the following optimization problem:

$$\begin{aligned} & \text{Argmin}_{d_k, i_k} \frac{1}{2} \left\| I - \sum_k (g_k^d \cdot d_k) \right\|_2^2 \\ & + \frac{1}{2} \left\| I - \sum_k (g_k^m \cdot m_k) \right\|_2^2 + \lambda \sum_k (\|d_k\|_1 + \|m_k\|_1) \end{aligned} \quad (5)$$

**Depth Feature Prediction Block (DFB)** The goal of DTB is used to compute the depth feature. According to [7], we fix  $m_k$  to update  $d_k$  by rewriting Eq. (5) as:

$$\text{Argmin}_{d_k} \frac{1}{2} \left\| E - \sum_k (g_k^d \cdot d_k) \right\|_2^2 + \lambda \sum_k \|d_k\|_1 \quad (6)$$

Eq. (6) is a standard convolutional sparse coding problem that can be solved using LCSC [29] by rewriting Eq. (6) as:

$$D_{j+1} = S_\lambda (D_j - L_d \cdot C_d \cdot D_j + L_d \cdot E) \quad (7)$$

where  $D \in \mathbb{R}^{H \times W \times K}$  is the stack of feature responses  $\{d^k\}_{k=1}^K$ ,  $D_j$  is the update of  $D$  at the  $j$ -th iteration,  $C_d \in \mathbb{R}^{s \times s \times K}$  and  $L_d \in \mathbb{R}^{s \times s \times K}$  are the learnable convolutional layers related to the filters  $\{g_k^d\}_{k=1}^K$ , and  $S_\lambda$  represents the soft thresholding operator. According to LCSC, we can expand the iterations in Eq. (7) into a neural network as shown in the framework in Fig. 3.

**Illumination Feature Prediction Block (IFB)** The goal of IFB is to compute the illuminance feature in a hazy image, the structure of this network is similar to that of DFB. By fixing  $d_k$  to update  $m_k$ , Eq. (5) can be rewritten as:

$$\text{Argmin}_{m_k} \frac{1}{2} \left\| E - \sum_k g_k^d \cdot m_k \right\|_2^2 + \lambda \sum_k \|m_k\|_1 \quad (8)$$

By using LCSC to solve the above problem, Eq. (8) can be rewritten as follows:

$$M_{j+1} = S_\lambda (M_j - L_m \cdot C_m \cdot M_j + L_m \cdot E) \quad (9)$$

where  $M \in \mathbb{R}^{H \times W \times K}$  is the stack of feature responses  $\{m^k\}_{k=1}^K$ ,  $M_j$  is the update of  $M$  at the  $j$ -th iteration, and  $C_m \in \mathbb{R}^{s \times s \times K}$  and  $L_m \in \mathbb{R}^{s \times s \times K}$  are the learnable convolutional layers related to the filters  $\{g_k^m\}_{k=1}^K$ . The network structure of the IFB is shown in Fig. 3.

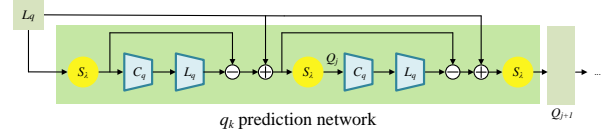


Figure 3. Network structure of DFB, IFB, and SFB.  $q_k \in \{d_k, m_k, s_{I,k}, s_{V,k}\}$  and  $Q_j \in \{D_j, M_j, S_j^I, S_j^V\}$ .

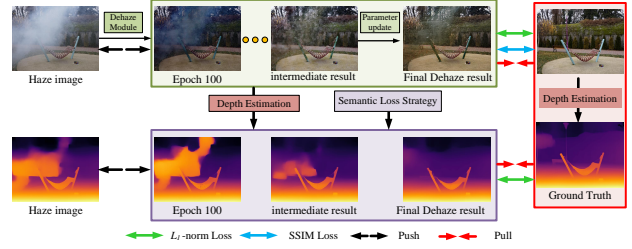


Figure 4. Description of the total loss function  $\mathcal{L}_{\text{dewather}}$  of the teacher deweathering module.

### 3.1.2 Loss Function for The Deweathering Module

Depth estimation can provide us with important information regarding the distance relationship between different objects in an image and the camera. As shown in Fig. 4, degraded image suffers from a lack of basic depth information in the scene. Image deweathering is performed to restore the clear details and depth of an image. To this end, a depth-estimation algorithm [27] is introduced for semantic loss in the training of the teacher model. The total loss function can be calculated as follows:

$$\mathcal{L}_{\text{dewather}} = \mathcal{L}_{\text{depth}} + \mathcal{L}_{\text{ssim}} + \mathcal{L}_{11} \quad (10)$$

where  $\mathcal{L}_{\text{depth}} = \|Z_{de} - Z_{gt}\|_1$  represents the semantic loss,  $Z_{gt}$  and  $Z_{de}$  represents the depth estimation maps of ground truth  $I_{gt}$  and deweathering image  $I_{de}$  respectively.  $\|\cdot\|_1$  denotes the  $L_1$ -norm,  $\mathcal{L}_{\text{ssim}}$  and  $\mathcal{L}_{11}$  represents the loss of structural similarity (SSIM) [35] and  $L_1$ -norm between  $I_{gt}$  and  $I_{de}$ , respectively. After training the three teacher models for the rain, haze, and snow weather, collaborative knowledge transfer [5] is used to enable the student models to be able to learn and organize the knowledge from the teachers.

### 3.1.3 Network Architecture for Image Deweathering

As shown in Fig. 2, the deweathering module in the model uses a U-Net backbone. In the backbone network, we stack five sparse transformer blocks (STB) to extract useful features distributed in adverse weather. STB mainly consist of top-k sparse attention (TKSA) and mixed-scale feed-forward network (MSFN). Regarding TKSA, it performs

feature aggregation to keep the features in an image sparse, and MSFN extracts multiscale local information from the image [6]. The proposed PFB focuses on refining the spatial information, which is embedded into both sides of the backbone network and enforced before being inputted into subsequent modules, to support image blurring, which helps recover the detailed information of an image.

### 3.2. Image Fusion Module

This section describes the main components of the fusion network. To effectively distinguish private and shared features from different modalities and thereby allow the fusion network to overcome the limitations in using a single encoder, a LLRR block is introduced. This block decomposes the source image into a low-rank component, which captures global structural information with high pixel correlation, and a sparse component, which represents high-frequency information with faster pixel variations. This approach enables the targeted handling of specific modal features and enhances fusion outcomes. Additionally, a sparse feature prediction block (SFB) is proposed to fuse sparse features in different modal images.

#### 3.2.1 SFB

Sparse feature fusion is performed to effectively extract and integrate local features specific to an infrared image  $I_r$  and a visible image  $Vis$ . The fused feature map  $\tilde{\mathbf{Z}}$  consists of two parts: the sparse feature  $S_{I,k} \in \mathbb{R}^{H \times W \times K}$  for  $I_r$  and the sparse feature  $S_{V,k} \in \mathbb{R}^{H \times W \times K}$  for  $Vis$ .  $\tilde{\mathbf{Z}}$  is modeled as follows:

$$\tilde{\mathbf{Z}} = \sum_k g_k^{S_I} \cdot s_{I,k} + \sum_k g_k^{S_V} \cdot s_{V,k} \quad (11)$$

where  $\{g_k^{S_I}\}_{k=1}^K \in \mathbb{R}^{s \times s \times K}$  and  $\{g_k^{S_V}\}_{k=1}^K \in \mathbb{R}^{s \times s \times K}$  are the sparse filters of  $z$  related to  $I_r$  and  $Vis$ , respectively. Subsequently, Eq. (11) can be transformed into the following optimization problem:

$$\begin{aligned} & \text{Argmin}_{S_I^I, S_V^V} \frac{1}{2} \left\| I_r - \sum_k (g_k^{S_I} \cdot S_{I,k}) \right\|_2^2 \\ & + \frac{1}{2} \left\| Vis - \sum_k (g_k^{S_V} \cdot S_{V,k}) \right\|_2^2 + \lambda \sum_k (\|S_{I,k}\|_1 + \|S_{V,k}\|_1) \end{aligned} \quad (12)$$

Similar to DFB and IFB,  $S_{I,k}$  and  $S_{V,k}$  are solved as follows:

$$S_{j+1}^I = S_\lambda(S_j^I - L_{S_I} \cdot C_{S_I} \cdot S_j^I + L_{S_I} \cdot I_r) \quad (13)$$

$$S_{j+1}^V = S_\lambda(S_j^V - L_{S_V} \cdot C_{S_V} \cdot S_j^V + L_{S_V} \cdot Vis) \quad (14)$$

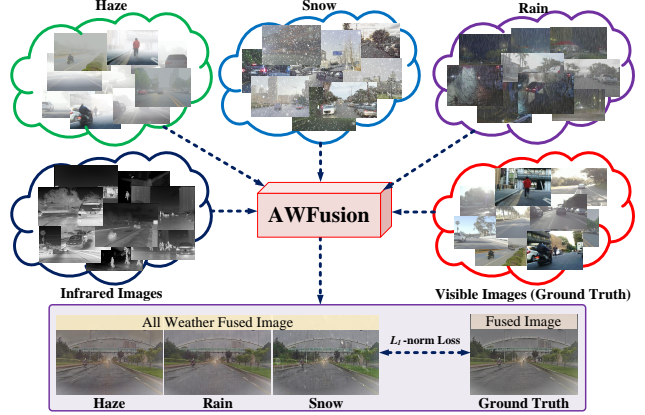


Figure 5. Schematic representation of the APLS.

where  $S_I \in \mathbb{R}^{H \times W \times K}$  and  $S_V \in \mathbb{R}^{H \times W \times K}$  are the stack of feature responses  $\{S_{I,k}\}_{k=1}^K$  and  $\{S_{V,k}\}_{k=1}^K$  respectively;  $S_j^I$  and  $S_j^V$  are the updates of  $S^I$  and  $S^V$  at the  $j$ -th iteration, respectively; and  $C_{S_I} \in \mathbb{R}^{s \times s \times K}$ ,  $C_{S_V} \in \mathbb{R}^{s \times s \times K}$ ,  $L_{S_I} \in \mathbb{R}^{s \times s \times K}$  and  $L_{S_V} \in \mathbb{R}^{s \times s \times K}$  are the learnable convolutional layers.

#### 3.2.2 Loss Function for Image Fusion Module

Considering the intricate nature of real-world scenes, deweathered images may exhibit subtle interferences. To enable the fusion module to filter problematic pixels autonomously, an advanced APLS, which is depicted in Fig. 5, is proposed. This strategy empowers the network to effectively eliminate interfering pixels during the fusion process, resulting in the improved retention of relevant scene details. The inclusion of  $L_1$ -norm, SSIM, and gradient loss function in the fusion algorithm aims to comprehensively evaluate and optimize the generated results by quantifying the structural similarity. The total loss  $\mathcal{L}_{\text{fusion}}$  of the fusion network is expressed as:

$$\mathcal{L}_{\text{fusion}} = \mathcal{L}_{l1} + \mathcal{L}_{\text{ssim}} + \mathcal{L}_{\text{gradient}} + \mathcal{L}_{\text{learn}} \quad (15)$$

where  $\mathcal{L}_{l1}$ ,  $\mathcal{L}_{\text{ssim}}$ ,  $\mathcal{L}_{\text{gradient}}$  and  $\mathcal{L}_{\text{learn}}$  represent the  $L_1$ -norm, SSIM, gradient, and anti-interference interactive perceptual learning loss, respectively.

#### 3.2.3 Network Architecture for Image Fusion

Fig. 2 shows the architecture of the proposed image fusion module. To distinguish between local and global information in different modal images, the LLRR block, which decomposes the source images into low-rank and sparse components, is incorporated. The long-range contextual feature extraction capability of the STB facilitates the fusion of the low-rank components that contain the most global information. Additionally, the SFB is designed to extract local

sparse features, which can perform a valuable fusion of the decomposed sparse separation. Finally, the fused low-rank and sparse components are combined to generate the final fused result.

### 3.2.4 MMIF Benchmark for Adverse Weather

Current MMIF datasets lack comprehensive scene coverage under severe weather. Combining existing datasets (RoadScene[38], MSRS[31], M3FD[20], and LLVIP[12]) and our newly collected data, we have established a substantial benchmark dataset AWMM-100k, which encompasses a diverse range of weather conditions and scene types. Each type of weather (rain, haze, and snow) is categorized into large, medium, and small levels. The images generation process is illustrated in Fig. 2. We employ a phenomenological pipeline [36] to introduce haze into source images, while rain and snow images are generated using Photoshop software utilizing masks based approach [4]. Moreover, this benchmark provides labels for two additional downstream tasks: object detection and semantic segmentation. These attributes render it a versatile resource for investigating a broad spectrum of visual tasks.

## 4. Experiment

### 4.1. Experimental configurations

We performed fusion experiments on the AWMM-100k dataset under adverse weather (haze, rain, and snow). The study included six state-of-the-art (SOTA) IVIF algorithms (CDDFuse[43], LRRNet[16], ReCoNet[11], SEAFusion[30], TarDAL[20], TGFuse[28]) with added baselines for haze, rain, and snow removal. The baseline A (KD) [5] addressed all three weather types, while baselines B (C2PNet) [44], C (DRSformer) [6], and D (HDCWNet) [4] addressed specific weather removal tasks (haze, rain, and snow). We chose 10 metrics to quantitatively evaluate different fusion results:  $Q_{MI}$ ,  $Q_P$ ,  $Q_{CB}$ ,  $Q_{CV}$ , visual information fidelity (VIF), average gradient (AG), spatial frequency (SF), Peak signal-to-noise ratio (PSNR), SSIM, and  $Q^{AB/F}$  [21]. All metrics except  $Q_{CV}$  are better as higher.

### 4.2. Training Details

For the deweathering process, three specialized teacher networks and one student network were trained under different weather conditions. During deweathering, 1000 visible light images from AWMM-100k were utilized as the teacher network training set, and each image was randomly cropped to  $160 \times 160$  to form batches. The Adam optimizer was employed with an initial learning rate of  $1 \times 10^{-3}$ , and the epoch was set to 300 for model training. In the knowledge-transfer phase, the teacher network was fixed, and the student network was trained for 250 epochs using a training

set featuring a mix of three weather types. After the student network was fixed, the fusion network was trained using 500 pairs of infrared and visible images containing rain, haze, and snow. These images were fed into the fusion network after being processed by the student network. All the experiments were conducted using the PyTorch framework on a system equipped with four NVIDIA 3090 GPUs.

## 4.3. Qualitative Comparison

### 4.3.1 Fusion Performance Comparison

Six sets of fusion experiments were conducted under three adverse weather, as shown in Fig. 6. The fusion results of various algorithms, accompanied by the visual analyses of two downstream tasks: salient object detection [26] and depth estimation [27], are illustrated in the figure.

In hazy scenes, the distribution of detail and semantic information was disrupted in the visible scene. All the contrast methods for baseline preprocessing could mitigate the interference caused by the haze-containing pixels to a certain extent. The red zoomed area shows that the three algorithms CDDFuse, LRRNet, and SEAFusion could reproduce most of the detailed information but that the contrast was still poor, and the detail distortion was large.

In rainy scenes, the raindrops introduced haziness and disrupted the distribution of detailed information. The fusion results from ReCoNet appeared dark, with an inadequate retention of details. However, the TarDAL method preserved excessive information from the infrared image, attempting to compensate for the incomplete removal of raindrops by the baseline. However, this method led to significant color distortion and loss of scene contrast.

In snowy scenes, the snow brightened the environment and obscured the targets and texture information. As indicated in the red zoomed area, CDDFuse, SEAFusion, and TGFuse methods excelled in preserving details but inevitably enhanced some of the luminance information related to snow. The TarDAL method assigned a greater weight to infrared information in the sky, resulting in the exclusion of snow but also the presence of scene distortions.

### 4.3.2 Downstream Task Performance Comparison

The results of the downstream tasks corresponding to each set of fusion experiments are shown in the second and fourth columns of Fig. 6. Clearly, each type of adverse weather significantly affected semantic information within a scene. The salient object detection results revealed that certain methods had consistently exhibited incomplete object detection (e.g., CDDFuse, TarDAL, and TGFuse) and that residual artifacts were present within the detected objects (e.g., ReCoNet and SEAFusion) owing to pixel interference induced by adverse weather. Regarding the depth estimation tasks, SEAFusion and TarDAL consistently offered

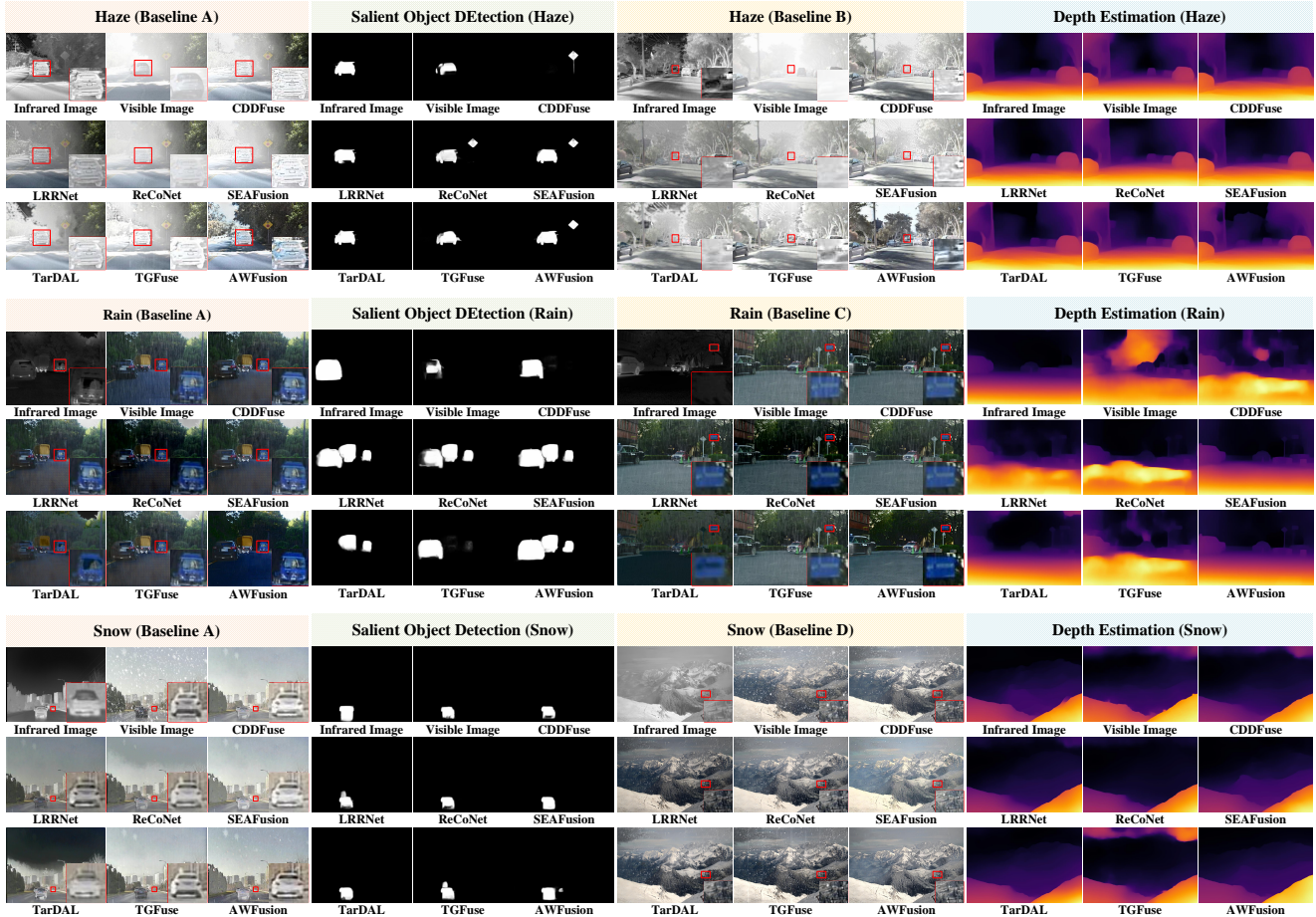


Figure 6. Fusion results of different algorithms on three adverse weather.

more accurate depth information than that offered by the other methods. However, due to weather interference, some distant trees and bushes might have been misestimated.

In summary, the proposed algorithm exhibited robust fusion performance across all three adverse weather scenarios, preserving rich details and semantic information while maintaining normal scene contrast. Notably, it achieved high-quality fusion under weather interference within a single framework, thereby eliminating the need for multiple preprocessing baselines.

#### 4.4. Quantitative Comparison

Tab. 1 presents the quantitative comparison results between the proposed algorithm and six comparative methods across three weather conditions. For each type of weather, 150 images from the AWMM-100k dataset were selected as a test set. Additionally, Baseline A was added to each algorithm. The table reveals that the proposed algorithm ranks in the top two for nine, nine, and seven metrics in the three adverse weather scenarios. This underscores its ability to deliver high-quality fusion results in challenging conditions,

effectively restoring disturbed pixel information within the scene and extracting salient target information from diverse modal images. In addition, SEAFusion and TarDAL methods also had top scores for several metrics.

Tab. 2 illustrates the quantitative results of target detection experiments. Nearly all methods demonstrated good detection outcomes. Tab. 2 highlights that the proposed method achieved the highest detection accuracy across five categories, underscoring its capability to provide high-quality semantic information even in adverse weather.

#### 4.5. Ablation Studies

To validate the impact of each component in our method we performed ablation studies. All experiments in this section were conducted in a haze scene. Tab. 3 presents the scores from the ablation study on five metrics for all algorithms.

**Effectiveness of Fusion Strategy.** We design different fusion rules after sparse and low-rank decomposition. To validate the efficacy of our proposed strategy, we selectively remove and interchange these fusion rules within the AW-Fusion model. As depicted in Tab. 3, each ablation algo-

Table 1. Quantitative comparison results of all algorithms in three weather conditions. **Bold** is the best and **red** is the second.

Method	Venue&Year	RAIN									
		$Q_{MI} \uparrow$	$Q_P \uparrow$	$Q_{CB} \uparrow$	$Q_{CV} \downarrow$	$VIF \uparrow$	$AG \uparrow$	$SF \uparrow$	$PSNR \uparrow$	$SSIM \uparrow$	$Q^{AB/F} \uparrow$
CDDFuse	<i>CVPR 2023</i>	0.3223	0.1682	0.4325	514.3126	0.1992	3.9070	<b>10.1188</b>	16.2830	<b>0.3563</b>	0.3789
LRRNet	<i>TPAMI 2023</i>	0.2647	0.0972	0.4154	817.1457	0.1493	3.2574	8.2860	15.2905	0.2553	0.2789
ReCoNet	<i>ECCV 2022</i>	0.2585	0.1442	0.3881	541.0537	0.2165	2.4776	7.5133	<b>19.1146</b>	0.1513	0.3049
SEAFusion	<i>Inf 2022</i>	<b>0.3286</b>	<b>0.1764</b>	<b>0.4386</b>	<b>505.6206</b>	0.2087	<b>3.9758</b>	10.0150	15.7892	<b>0.3696</b>	0.3900
TarDAL	<i>CVPR 2022</i>	0.2874	0.1151	0.3873	2191.1577	<b>0.2174</b>	2.6931	8.4672	15.5988	0.3395	0.2151
TGFuse	<i>TIP 2023</i>	0.2485	0.1527	0.4334	696.4563	0.1887	3.8316	9.7537	15.6706	0.3346	<b>0.3931</b>
AWFusion	<b>Propose</b>	<b>0.3758</b>	<b>0.2045</b>	<b>0.4549</b>	<b>438.4218</b>	<b>0.2264</b>	<b>4.1565</b>	<b>12.0719</b>	<b>16.5858</b>	0.3089	<b>0.4096</b>
HAZE											
CDDFuse	<i>CVPR 2023</i>	0.2732	0.3205	0.3523	815.3318	0.3184	4.5259	<b>13.1791</b>	10.4166	0.3323	0.4177
LRRNet	<i>TPAMI 2023</i>	0.2520	0.2345	0.3544	1075.0016	0.2813	3.2992	9.2286	11.9375	0.2443	0.3115
ReCoNet	<i>ECCV 2022</i>	0.2704	0.2521	0.3372	878.3330	<b>0.3370</b>	3.4322	9.0467	11.3826	0.2822	0.3138
SEAFusion	<i>Inf 2022</i>	0.2690	0.3048	0.3601	<b>783.0397</b>	0.3142	<b>4.5808</b>	12.3850	10.4160	<b>0.3474</b>	0.4342
TarDAL	<i>CVPR 2022</i>	<b>0.3177</b>	0.2045	<b>0.3966</b>	2251.4079	0.2993	3.4682	12.9468	<b>12.3269</b>	0.3089	0.2493
TGFuse	<i>TIP 2023</i>	0.2463	<b>0.3266</b>	0.3809	931.5368	<b>0.3226</b>	4.2915	12.1280	10.2419	0.3086	<b>0.4376</b>
AWFusion	<b>Propose</b>	<b>0.3167</b>	<b>0.3405</b>	<b>0.4374</b>	<b>553.9969</b>	0.2569	<b>6.0756</b>	<b>17.2219</b>	<b>12.9994</b>	<b>0.3746</b>	<b>0.4771</b>
SNOW											
CDDFuse	<i>CVPR 2023</i>	0.3071	<b>0.1141</b>	0.4208	604.5829	0.1391	<b>5.2398</b>	<b>12.6114</b>	12.5098	0.2557	0.3271
LRRNet	<i>TPAMI 2023</i>	0.2722	0.1006	0.4085	921.9993	<b>0.1492</b>	3.7164	9.0592	<b>14.6656</b>	0.2098	0.2487
ReCoNet	<i>ECCV 2022</i>	0.2911	0.1021	0.4038	648.0484	0.1451	4.2688	9.7812	13.7680	0.2406	0.2739
SEAFusion	<i>Inf 2022</i>	0.3126	<b>0.1219</b>	0.4208	<b>541.1084</b>	0.1485	5.0556	12.0869	12.1790	0.2624	<b>0.3305</b>
TarDAL	<i>CVPR 2022</i>	<b>0.3961</b>	0.1123	0.3955	1355.2252	<b>0.2165</b>	2.7858	8.1714	<b>13.8227</b>	<b>0.2704</b>	0.1773
TGFuse	<i>TIP 2023</i>	0.2772	0.1131	<b>0.4265</b>	972.7522	0.1379	4.7494	11.5141	12.0346	0.2171	0.3295
AWFusion	<b>Propose</b>	<b>0.3148</b>	0.1023	<b>0.4255</b>	<b>551.8158</b>	0.1074	<b>6.7082</b>	<b>15.4840</b>	13.4815	<b>0.5607</b>	<b>0.3345</b>

algorithm results in a performance degradation compared to the original AWFusion model, affirming the targeted design rationale behind our fusion rules.

**Effectiveness of APLS.** We proposed APLS to enable the fusion module to proactively eliminate interfering pixels, we assess its efficacy in this section. The outcomes depicted in Tab. 3 distinctly affirm the effectiveness of the proposed APLS for the model. Following training with this strategy, the model exhibits anti-interference capabilities, leading to improved performance across all five presented metrics.

Table 2. Quantitative results of object detection on rain scene among all the image fusion methods + detector (YOLOv7 [34]).

Method	People	Car	Bus	Traffic Light	Lamp	Truck	mAP@.5
CDDFuse	0.831	0.908	<b>0.927</b>	0.809	<b>0.690</b>	<b>0.872</b>	<b>0.839</b>
LRRNet	0.763	0.906	0.910	<b>0.827</b>	0.687	0.853	0.825
ReCoNet	0.763	0.906	0.910	<b>0.827</b>	0.687	0.853	0.825
SEAFusion	<b>0.847</b>	<b>0.911</b>	0.915	0.824	0.660	0.847	0.838
TarDAL	0.766	0.872	0.847	0.670	0.643	0.789	0.764
TGFuse	0.801	0.908	0.889	0.808	<b>0.695</b>	<b>0.856</b>	0.826
AWFusion	<b>0.840</b>	<b>0.919</b>	<b>0.943</b>	<b>0.842</b>	0.650	<b>0.872</b>	<b>0.844</b>

## 5. Discussion

**Conclusion.** In this study, we introduced an all-weather IVIF network. Specially, an deweathering module was designed to recover the clear details obscured by interfer-

Table 3. Validation for effectiveness of STB, SFB and APLS, where AWFusion-A, -B, -C, and -E represent the proposed model without SFB, STB, both SFB and STB, and APLS respectively. AWFusion-D denotes the model acquired by swapping the SFB and STB in the original method.

Method	$Q_{MI} \uparrow$	$Q_{CB} \uparrow$	$VIF \uparrow$	$AG \uparrow$	$SF \uparrow$
AWFusion-A	0.4556	0.4384	0.2208	6.9941	19.3947
AWFusion-B	0.4245	0.4445	0.2178	7.0080	19.9109
AWFusion-C	0.4367	0.4360	0.2118	7.2869	19.5910
AWFusion-D	0.4260	0.4437	0.2140	7.0478	20.0222
AWFusion-E	0.4072	0.4419	0.2034	7.4976	21.3642
Proposed	<b>0.4982</b>	<b>0.4816</b>	<b>0.2341</b>	<b>7.6885</b>	<b>23.0162</b>

ence pixels and then, an FFP was proposed to predict clear feature information accurately. We also proposed a fusion module grounded in sparse and low-rank separation to amalgamate information from infrared and visible images across distinct modalities. Experimental results demonstrate the proposed AWFusion excel existing methods in adverse weather fusions.

**Limitations and Future Work.** The algorithm, facing concurrent disturbances like rain and snow, shows limitations in fully eliminating disturbance information.

## 6. Acknowledgements

This research was supported in part by the National Natural Science Foundation of China under Grant 62201149, in part by the Guangdong Higher Education Innovation and Strengthening of Universities Project under Grant 2023KTSCX127, and in part by the Foshan Key Areas of Scientific and Technological Research Project under Grant 2120001008558.

## References

- [1] Alexey Bochkovskiy, Chien-Yao Wang, and Hong-Yuan Mark Liao. Yolov4: Optimal speed and accuracy of object detection. *arXiv preprint arXiv:2004.10934*, 2020. 1
- [2] Liang-Chieh Chen, George Papandreou, Iasonas Kokkinos, Kevin Murphy, and Alan L Yuille. Deeplab: Semantic image segmentation with deep convolutional nets, atrous convolution, and fully connected crfs. *IEEE transactions on pattern analysis and machine intelligence*, 40(4):834–848, 2017. 1
- [3] Liang-Chieh Chen, Yukun Zhu, George Papandreou, Florian Schroff, and Hartwig Adam. Encoder-decoder with atrous separable convolution for semantic image segmentation. In *Proceedings of the European conference on computer vision (ECCV)*, pages 801–818, 2018. 1
- [4] Wei-Ting Chen, Hao-Yu Fang, Cheng-Lin Hsieh, Cheng-Che Tsai, I Chen, Jian-Jiun Ding, Sy-Yen Kuo, et al. All snow removed: Single image desnowing algorithm using hierarchical dual-tree complex wavelet representation and contradict channel loss. In *Proceedings of the IEEE/CVF International Conference on Computer Vision*, pages 4196–4205, 2021. 6
- [5] Wei-Ting Chen, Zhi-Kai Huang, Cheng-Che Tsai, Hao-Hsiang Yang, Jian-Jiun Ding, and Sy-Yen Kuo. Learning multiple adverse weather removal via two-stage knowledge learning and multi-contrastive regularization: Toward a unified model. In *Proceedings of the IEEE/CVF Conference on Computer Vision and Pattern Recognition*, pages 17653–17662, 2022. 3, 4, 6
- [6] Xiang Chen, Hao Li, Mingqiang Li, and Jinshan Pan. Learning a sparse transformer network for effective image deraining. In *Proceedings of the IEEE/CVF Conference on Computer Vision and Pattern Recognition*, pages 5896–5905, 2023. 2, 5, 6
- [7] Xin Deng and Pier Luigi Dragotti. Deep convolutional neural network for multi-modal image restoration and fusion. *IEEE transactions on pattern analysis and machine intelligence*, 43(10):3333–3348, 2020. 2, 4
- [8] Jiangxin Dong and Jinshan Pan. Physics-based feature dehazing networks. In *Computer Vision—ECCV 2020: 16th European Conference, Glasgow, UK, August 23–28, 2020, Proceedings, Part XXX 16*, pages 188–204. Springer, 2020. 2
- [9] Yu Fu, Xiao-Jun Wu, and Tariq Durrani. Image fusion based on generative adversarial network consistent with perception. *Information Fusion*, 72:110–125, 2021. 2
- [10] Mina Han, Kailong Yu, Junhui Qiu, Hao Li, Dan Wu, Yujing Rao, Yang Yang, Lin Xing, Haicheng Bai, and Chengjiang Zhou. Boosting target-level infrared and visible image fusion with regional information coordination. *Information Fusion*, 92:268–288, 2023. 2
- [11] Zhanbo Huang, Jinyuan Liu, Xin Fan, Risheng Liu, Wei Zhong, and Zhongxuan Luo. Reconet: Recurrent correction network for fast and efficient multi-modality image fusion. In *European Conference on Computer Vision*, pages 539–555. Springer, 2022. 3, 6
- [12] Xinyu Jia, Chuang Zhu, Minzhen Li, Wenqi Tang, and Wenli Zhou. Llvip: A visible-infrared paired dataset for low-light vision. In *Proceedings of the IEEE/CVF international conference on computer vision*, pages 3496–3504, 2021. 6
- [13] Lihua Jian, Xiaomin Yang, Zheng Liu, Gwanggil Jeon, Mingliang Gao, and David Chisholm. Sedrfuse: A symmetric encoder–decoder with residual block network for infrared and visible image fusion. *IEEE Transactions on Instrumentation and Measurement*, 70:1–15, 2020. 2
- [14] Zhuliang Le, Jun Huang, Han Xu, Fan Fan, Yong Ma, Xiaoguang Mei, and Jiayi Ma. Uifgan: An unsupervised continual-learning generative adversarial network for unified image fusion. *Information Fusion*, 88:305–318, 2022. 2
- [15] Huafeng Li, Yueliang Cen, Yu Liu, Xun Chen, and Zhengtao Yu. Different input resolutions and arbitrary output resolution: A meta learning-based deep framework for infrared and visible image fusion. *IEEE Transactions on Image Processing*, 30:4070–4083, 2021. 3
- [16] Hui Li, Tianyang Xu, Xiao-Jun Wu, Jiwen Lu, and Josef Kittler. Lrrnet: A novel representation learning guided fusion network for infrared and visible images. *IEEE transactions on pattern analysis and machine intelligence*, 2023. 1, 2, 6
- [17] Jiawei Li, Jiansheng Chen, Jinyuan Liu, and Huimin Ma. Learning a graph neural network with cross modality interaction for image fusion. In *Proceedings of the 31st ACM International Conference on Multimedia*, pages 4471–4479, 2023. 2
- [18] Jiale Li, Hang Dai, Hao Han, and Yong Ding. Mseg3d: Multi-modal 3d semantic segmentation for autonomous driving. In *Proceedings of the IEEE/CVF Conference on Computer Vision and Pattern Recognition*, pages 21694–21704, 2023. 1
- [19] Pengwei Liang, Junjun Jiang, Xianming Liu, and Jiayi Ma. Fusion from decomposition: A self-supervised decomposition approach for image fusion. In *European Conference on Computer Vision*, pages 719–735. Springer, 2022. 2
- [20] Jinyuan Liu, Xin Fan, Zhanbo Huang, Guanyao Wu, Risheng Liu, Wei Zhong, and Zhongxuan Luo. Target-aware dual adversarial learning and a multi-scenario multi-modality benchmark to fuse infrared and visible for object detection. In *Proceedings of the IEEE/CVF Conference on Computer Vision and Pattern Recognition*, pages 5802–5811, 2022. 1, 2, 6
- [21] Jiayi Ma, Yong Ma, and Chang Li. Infrared and visible image fusion methods and applications: A survey. *Information fusion*, 45:153–178, 2019. 1, 6
- [22] Jiayi Ma, Wei Yu, Pengwei Liang, Chang Li, and Junjun Jiang. Fusiongan: A generative adversarial network for infrared and visible image fusion. *Information fusion*, 48:11–26, 2019. 2

- [23] Jiayi Ma, Hao Zhang, Zhenfeng Shao, Pengwei Liang, and Han Xu. Ganncc: A generative adversarial network with multiclassification constraints for infrared and visible image fusion. *IEEE Transactions on Instrumentation and Measurement*, 70:1–14, 2020. 2
- [24] Jiayi Ma, Linfeng Tang, Fan Fan, Jun Huang, Xiaoguang Mei, and Yong Ma. Swinfusion: Cross-domain long-range learning for general image fusion via swin transformer. *IEEE/CAA Journal of Automatica Sinica*, 9(7):1200–1217, 2022. 2
- [25] Nirmala Paramanandham and Kishore Rajendiran. Infrared and visible image fusion using discrete cosine transform and swarm intelligence for surveillance applications. *Infrared Physics & Technology*, 88:13–22, 2018. 1
- [26] Xuebin Qin, Zichen Zhang, Chenyang Huang, Masood Dehghan, Osmar R Zaiane, and Martin Jagersand. U2-net: Going deeper with nested u-structure for salient object detection. *Pattern recognition*, 106:107404, 2020. 6
- [27] René Ranftl, Katrin Lasinger, David Hafner, Konrad Schindler, and Vladlen Koltun. Towards robust monocular depth estimation: Mixing datasets for zero-shot cross-dataset transfer. *IEEE transactions on pattern analysis and machine intelligence*, 44(3):1623–1637, 2020. 4, 6
- [28] Dongyu Rao, Tianyang Xu, and Xiao-Jun Wu. Tgfuse: An infrared and visible image fusion approach based on transformer and generative adversarial network. *IEEE Transactions on Image Processing*, 2023. 6
- [29] Hillel Sreter and Raja Giryes. Learned convolutional sparse coding. In *2018 IEEE International Conference on Acoustics, Speech and Signal Processing (ICASSP)*, pages 2191–2195. IEEE, 2018. 2, 4
- [30] Linfeng Tang, Jiteng Yuan, and Jiayi Ma. Image fusion in the loop of high-level vision tasks: A semantic-aware real-time infrared and visible image fusion network. *Information Fusion*, 82:28–42, 2022. 2, 6
- [31] Linfeng Tang, Jiteng Yuan, Hao Zhang, Xingyu Jiang, and Jiayi Ma. Piafusion: A progressive infrared and visible image fusion network based on illumination aware. *Information Fusion*, 83:79–92, 2022. 6
- [32] Wei Tang, Fazhi He, and Yu Liu. Tccfusion: An infrared and visible image fusion method based on transformer and cross correlation. *Pattern Recognition*, 137:109295, 2023. 2
- [33] Vibashan VS, Poojan Oza, and Vishal M Patel. Towards online domain adaptive object detection. In *Proceedings of the IEEE/CVF Winter Conference on Applications of Computer Vision*, pages 478–488, 2023. 1
- [34] Chien-Yao Wang, Alexey Bochkovskiy, and Hong-Yuan Mark Liao. Yolov7: Trainable bag-of-freebies sets new state-of-the-art for real-time object detectors. In *Proceedings of the IEEE/CVF Conference on Computer Vision and Pattern Recognition*, pages 7464–7475, 2023. 1, 8
- [35] Zhou Wang, Alan C Bovik, Hamid R Sheikh, and Eero P Simoncelli. Image quality assessment: from error visibility to structural similarity. *IEEE transactions on image processing*, 13(4):600–612, 2004. 4
- [36] Rui-Qi Wu, Zheng-Peng Duan, Chun-Le Guo, Zhi Chai, and Chongyi Li. Ridcp: Revitalizing real image dehazing via high-quality codebook priors. In *Proceedings of the IEEE/CVF Conference on Computer Vision and Pattern Recognition*, pages 22282–22291, 2023. 6
- [37] Yi Xiao, Felipe Codevilla, Akhil Gurram, Onay Urfalioglu, and Antonio M López. Multimodal end-to-end autonomous driving. *IEEE Transactions on Intelligent Transportation Systems*, 23(1):537–547, 2020. 1
- [38] Han Xu, Jiayi Ma, Junjun Jiang, Xiaojie Guo, and Haibin Ling. U2fusion: A unified unsupervised image fusion network. *IEEE Transactions on Pattern Analysis and Machine Intelligence*, 44(1):502–518, 2020. 2, 6
- [39] Han Xu, Jiteng Yuan, and Jiayi Ma. Murf: Mutually reinforcing multi-modal image registration and fusion. *IEEE Transactions on Pattern Analysis and Machine Intelligence*, 2023. 3
- [40] Meilong Xu, Linfeng Tang, Hao Zhang, and Jiayi Ma. Infrared and visible image fusion via parallel scene and texture learning. *Pattern Recognition*, 132:108929, 2022. 2
- [41] Fan Zhao, Wenda Zhao, and Huchuan Lu. Interactive feature embedding for infrared and visible image fusion. *IEEE Transactions on Neural Networks and Learning Systems*, 2023. 2
- [42] Zixiang Zhao, Shuang Xu, Jianshe Zhang, Chengyang Liang, Chunxia Zhang, and Junmin Liu. Efficient and model-based infrared and visible image fusion via algorithm unrolling. *IEEE Transactions on Circuits and Systems for Video Technology*, 32(3):1186–1196, 2021. 2
- [43] Zixiang Zhao, Haowen Bai, Jianshe Zhang, Yulun Zhang, Shuang Xu, Zudi Lin, Radu Timofte, and Luc Van Gool. Cddfuse: Correlation-driven dual-branch feature decomposition for multi-modality image fusion. In *Proceedings of the IEEE/CVF Conference on Computer Vision and Pattern Recognition*, pages 5906–5916, 2023. 1, 2, 6
- [44] Yu Zheng, Jiahui Zhan, Shengfeng He, Junyu Dong, and Yong Du. Curricular contrastive regularization for physics-aware single image dehazing. In *Proceedings of the IEEE/CVF Conference on Computer Vision and Pattern Recognition*, pages 5785–5794, 2023. 2, 3, 6
- [45] Huabing Zhou, Wei Wu, Yanduo Zhang, Jiayi Ma, and Haibin Ling. Semantic-supervised infrared and visible image fusion via a dual-discriminator generative adversarial network. *IEEE Transactions on Multimedia*, 2021. 2
- [46] Yurui Zhu, Tianyu Wang, Xueyang Fu, Xuanyu Yang, Xin Guo, Jifeng Dai, Yu Qiao, and Xiaowei Hu. Learning weather-general and weather-specific features for image restoration under multiple adverse weather conditions. In *Proceedings of the IEEE/CVF Conference on Computer Vision and Pattern Recognition*, pages 21747–21758, 2023. 2